DOI: 10.61782/fa.2023.1255

forum acusticum 2023

ACCURATE TIME-DOMAIN SIMULATION OF SPHERICAL MICROPHONE ARRAYS

Nara Hahn[1,2,*] **Frank Schultz**[2] **Sascha Spors**[2]
[1]Institute of Sound and Vibration Research, University of Southampton, United Kingdom
[2]Institute of Communications Engineering, University of Rostock, Germany

ABSTRACT

The simulation of spherical microphone arrays is commonly performed in the frequency domain using spherical harmonic representation of the spatial transfer functions. Each modal spectrum is described by the spherical Hankel function and its derivative. Although the resulting simulation is accurate in the frequency domain, the corresponding time-domain signal obtained by the inverse discrete Fourier transform (IDFT) exhibits temporal aliasing and smearing. Moreover, evaluating the spherical Hankel functions at a larger number of frequencies can be a computational bottleneck. In this paper, we propose a time-domain approach, where each modal transfer function is implemented as a parallel combination of IIR filters and a single FIR filter. The poles of the IIR filters correspond to the roots of the spherical Hankel functions' derivatives, which can be pre-computed for a given radius. The FIR filter coefficients are obtained by the least-squares solution, where the squared spectrum errors are minimized at control frequencies. While the number of poles are fixed for each harmonic order, the FIR length is a free design parameter, with which the simulation accuracy can be adjusted. The presented approach is compared numerically with previously proposed time-domain methods and the frequency-domain modeling.

Keywords: *Spherical microphone array, rigid sphere, impulse invariance method, band-limited invariance method, parallel-structure filter, least squares solution*

[*] ***Corresponding author***: *nara.hahn@soton.ac.uk,*

1. INTRODUCTION

Rigid spherical microphone arrays are widely used for capturing sound fields [1–3]. Developing and evaluating associated signal processing techniques (e.g. Ambisonic encoding, beamforming, sound field analysis) often require numerical simulations of different configurations for various capturing scenarios [4, 5]. There are several factors that have to be considered for an accurate and reliable simulation, e.g. accuracy in the frequency domain, structure in the time domain, computational efficiency of the modeling, and computational efficiency of the simulation. Simulations in the frequency domain, for instance, achieve high accuracy in the frequency domain, but hardly meet the other three requirements.

The authors proposed a time-domain approach in [6], where the acoustic impulse responses are modeled with digital IIR filters. This method is inspired by earlier studies in array signal processing [7–10]. The filter coefficients are derived from an analytical representation of the system function. In comparison to the frequency-domain model, the computational complexity is reduced in both modeling and implementation. The resulting impulse responses exhibit compact transients and are free of temporal artifacts such as pre-ringing. One downside of the time-domain approach, though, is that the accuracy in the frequency domain is inferior. This is mainly attributed to frequency-domain aliasing.

An improved time-domain model is presented in [11], where the spectral aliasing is reduced by the band-limited impulse invariance method [12]. An FIR filter is added to the model in parallel to the IIR filters. The FIR filter is designed in such a way that it cancels the aliasing produced by the IIR filters. The FIR coefficients are derived analytically based on an ideally low-pass filtered im-

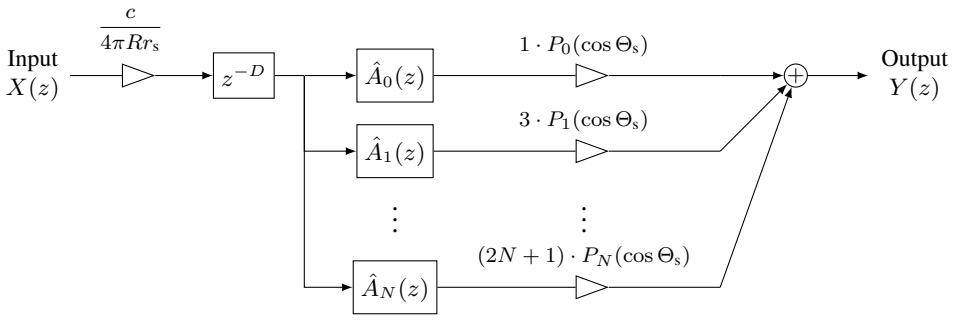

Figure 1. Discrete-time model (z-domain) of the acoustic transmission from a point source at (r_s, θ_s, ϕ_s) to a receiver on a rigid sphere (R, θ, ϕ) [cf. (9)]. The modal spectra are implemented as digital filters $\hat{A}_n(z)$ for $n = 0, 1, \ldots, N$.

pulse response of the system function. This leads to a closed-form expression described by the exponential integral function with an appropriate time-domain windowing. The FIR part slightly increases the computational complexity, but the proposed time-domain model is still more efficient than the frequency-domain approach.

In this paper, we introduce an extension of our model, where a numerical method is employed. Instead of relying on analytical representations, the least square solution is used for the FIR filter design which minimizes the spectral errors at predefined frequencies in the mean squared error sense. The same coefficients are used for the IIR part, and the overall filter structure remains unchanged. Therefore, the computational complexity of the simulation itself does not change. The new approach provides an alternative option for the time-domain model, where the error spectrum can be shaped differently depending on the distribution of the control frequencies.

The remainder of this paper is structured as follows. Section 2 presents the Laplace-domain formulation of the acoustic transfer function and reviews a recently introduced time-domain design approach. The proposed method is introduced in Sec. 3, describing the numerical design of the FIR filter. Section 4 demonstrates the improvements by simulation results. The paper is then concluded in Sec. 5.

Nomenclature Positions and directions are represented with spherical coordinates (r, θ, ϕ), where $r \geq 0$ denotes the radius in m, $\theta \in [0°, 180°]$ the colatitude, and $\phi \in [0°, 360°)$ the azimuth. Angular frequency in $\mathrm{rad/s}$ is denoted by $\omega = 2\pi f$ where f is the corresponding frequency in Hz. For a given sampling frequency f_s, the normalized angular frequency is denoted by $\Omega = \omega \cdot T_s$ with $T_s = \frac{1}{f_s}$ denoting the sampling interval in s. The time harmonic term $e^{i\omega t}$ is omitted for brevity. The speed of sound in $\mathrm{m/s}$ is denoted by c and the imaginary unit by i.

2. ANALYTICAL BAND LIMITED IMPULSE INVARIANCE METHOD

This section reviews the time-domain modeling of spherical microphone arrays presented in [6, 11]. We assume that a point source, positioned at $\boldsymbol{x}_s = (r_s, \theta_s, \phi_s)$, emits a spherical wave in a free field. The emitted sound field is captured on a rigid sphere with radius R centered at the origin. The captured sound field by a receiver at $\boldsymbol{x} = (R, \theta, \phi)$ can be expanded in terms of spherical modes as [13, Sec. 4.2]

$$S(\boldsymbol{x}, \omega) = \sum_{n=0}^{\infty} \frac{2n+1}{4\pi} P_n(\cos\Theta_s) \frac{-h_n(\frac{\omega}{c} r_s)}{\frac{\omega}{c} R^2 \cdot h_n'(\frac{\omega}{c} R)}. \quad (1)$$

The angular dependencies are described by the Legendre polynomials $P_n(\cos\Theta_s)$, where Θ_s denotes the angle between $\boldsymbol{x}$ and $\boldsymbol{x}_s$. The spectral and radial dependencies are described by the spherical Hankel function of the second kind $h_n(\cdot)$ and the derivative with respect to its argument $h_n'(\cdot)$. In the considered time-harmonic convention ($e^{i\omega t}$), the latter represent the outgoing waves (radiation from the point source and scattering by the sphere). The commonly used superscript $(\cdot)^{(2)}$ is omitted for brevity.

By exploiting the explicit formula of the spherical Hankel functions [14, Eq. (10.49.7)], the rational part in (1) can be expressed as

$$\frac{-h_n(\frac{\omega}{c} r_s)}{\frac{\omega}{c} R^2 \cdot h_n'(\frac{\omega}{c} R)} = \frac{c}{r_s R} e^{-i\frac{\omega}{c}(R - r_s)} A_n(i\omega), \quad (2)$$

with $A_n(i\omega)$ denoting the spectral component of each mode,

$$A_n(i\omega) = \frac{\sum_{k=0}^{n} \beta_n(k) \cdot (\frac{r_s}{c})^{k-n} \cdot (i\omega)^k}{\sum_{k=0}^{n+1} \gamma_n(k) \cdot (\frac{R}{c})^{k-n-1} \cdot (i\omega)^k}. \quad (3)$$

The coefficients $\beta_n(k)$ and $\gamma_n(k)$ are defined as

$$\beta_n(k) = \begin{cases} \frac{(2n-k)!}{(n-k)!k!2^{n-k}} & k = 0, 1, \ldots, n \\ 0, & \text{otherwise} \end{cases} \quad (4)$$

and

$$\gamma_n(k) = \begin{cases} \beta_{n+1}(k) - n \cdot \beta_n(k), & k = 0, 1, \ldots, n \\ 1, & k = n+1 \\ 0, & \text{otherwise}, \end{cases} \quad (5)$$

respectively [11].

The analytic continuation of (3) in the complex plane yields the Laplace-domain representation of the system function ($s \in \mathbb{C}$),

$$A_n(s) = \frac{\sum_{k=0}^{n} \beta_n(k) \cdot (\frac{r_s}{c})^{k-n} \cdot s^k}{\sum_{k=0}^{n+1} \gamma_n(k) \cdot (\frac{R}{c})^{k-n-1} \cdot s^k}. \quad (6)$$

As discussed in [11], each modal transfer function is characterized by n zeros and $n+1$ poles, all of which are distinct and lying on the left half of the complex plane. Equation (6) thus can be expressed as a factorized form,

$$A_n(s) = \frac{\prod_{k=0}^{n-1}(s - q_{n,k})}{\prod_{k=0}^{n}(s - p_{n,k})}, \quad (7)$$

where $q_{n,k}$ denotes the kth zero and $p_{n,k}$ the kth pole of the nth modal spectrum $A_n(s)$. Alternatively, $A_n(s)$ can be formulated as a partial fraction expansion,

$$A_n(s) = \sum_{k=0}^{n} \frac{\rho_{n,k}}{s - p_{n,k}}, \quad (8)$$

where $\rho_{n,k}$ denotes the kth residue corresponding to $p_{n,k}$.

The overall system function (Laplace domain) can be rewritten by plugging (2) into (1) yields

$$S(\boldsymbol{x}, s) = \frac{c \cdot e^{-\frac{r_s - R}{c} s}}{4\pi r_s R} \sum_{n=0}^{\infty} (2n+1) P_n(\cos\Theta_s) A_n(s). \quad (9)$$

Equation (9) consists of an overall amplitude scaling $\frac{c}{4\pi r_s R}$, an overall delay $e^{-\frac{r_s - R}{c} s}$, and a superposition of the modal transfer functions $A_n(s)$ weighted by the directional dependent parts $P_n(\cos\Theta_s)$. The linear-phase delay $e^{-\frac{r_s - R}{c} s}$ corresponds to the wave propagation from the source to the nearest point on the sphere. The relative delays between the individual receivers are modeled by $A_n(s)$ which have nonlinear phase responses.

For a numerical simulation of the sound field on the rigid sphere, the continuous-time system function (9) has to be discretized [cf. Fig. 1]. The overall delay can be realized with an integer-sample shift $D = \left[\frac{r_s - R}{c} T_s\right]$ where $[\cdot]$ denotes the rounding operator, or with a fractional delay filter [15] The latter might be desired if multiple sound sources are considered and a high temporal resolution is of importance. Note from Fig. 1 that the expansion (9) is truncated to the Nth order. The rule of thumb $N \geq \frac{\omega}{c} R$ is commonly used to determine the expansion order. The modal transfer function $A_n(s)$ is modeled by a discrete-time system whose z-transform is denoted by $\hat{A}_n(z)$. The linear time-invariant system is modeled by a digital filter which can be built either based on cascade (7) or partial fraction expansion formulation (8). Bilinear transform or matched z-transform can be used for the former, and impulse invariance method for the latter. The resulting discrete-time models typically exhibit spectral distortions due to frequency warping or frequency-domain aliasing [6].

The frequency-domain accuracy of the discrete-time model can be improved by using the band-limited impulse invariance method [11, 12]. It is based on the parallel model of continuous-time systems as described by (8). Since the system is supposed to be causal, the corresponding impulse response (inverse Laplace transform) is a sum of right-sided complex exponential functions,

$$a_n(t) = \sum_{k=0}^{n} \rho_{n,k} \cdot e^{p_{n,k} \cdot t} u(t), \quad (10)$$

with $u(t)$ denoting the Heaviside step function. The conventional impulse invariance method [16, 17] is based on time-domain sampling of the impulse response. The z-transform of the time-domain sampling of (10) reads

$$\hat{A}_n^{(\mathrm{II})}(z) = \sum_{k=0}^{n} \frac{\rho_{n,k} T_s}{2} \frac{1 + e^{p_{n,k} T_s} z^{-1}}{1 - e^{p_{n,k} T_s} z^{-1}}, \quad (11)$$

where the superscript 'II' indicates the impulse invariance method. While the temporal structure of the original impulse response is well modeled by the decaying exponential functions, the spectrum typically exhibits aliasing distortions. In the band-limited impulse invariance method,

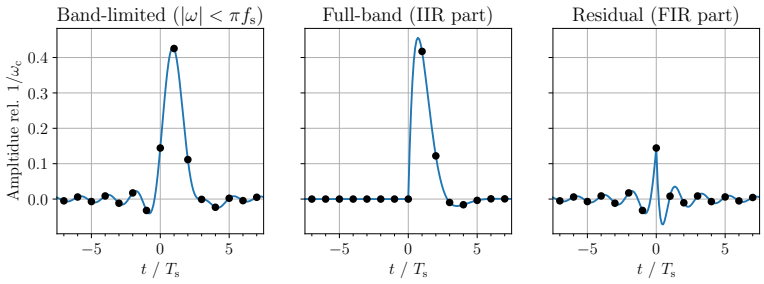

Figure 2. Impulse response of a 2nd-order Butterworth low-pass filter (sampling frequency $f_s = 48\,\mathrm{kHz}$, cut-off frequency $\omega_c = 2\pi f_c$ with $f_c = \frac{1}{4} f_s$, poles $p_{\{1,2\}} = \omega_c \cdot e^{\pm i \frac{3}{4}\pi}$, residues $\rho_{\{1,2\}} = \frac{\omega_c}{\sqrt{2}} \cdot e^{\mp i \frac{\pi}{2}}$). The band-limited impulse response in the first subplot is an ideally low-passed filtered version of the full-band impulse response shown in the second subplot. The third subplot depicts the difference between these two impulse responses. A discrete-time implementation of the band-limited impulse response can be performed by using the full-band part with an IIR filter and the residual with an FIR filter. The black circles indicate the discrete-time samples at $t = \mu T_s, \forall \mu \in \mathbb{Z}$. The amplitudes are normalized by the cut-off frequency ω_c and the time axis by the sampling period T_s.

an FIR filter is combined in parallel with the delayed IIR filter obtained in (11),

$$\hat{A}_n^{(\mathrm{ABL})}(z) = z^{-M} \cdot \hat{A}_n^{(\mathrm{II})}(z) + \sum_{l=0}^{L-1} d_{n,l}^{(\mathrm{ABL})} z^{-l}. \qquad (12)$$

The FIR coefficients $d_{n,k}^{(\mathrm{ABL})}$ are derived analytically based on the inverse Laplace transform of a band-limited ($|\omega| < \pi f_s$) version of (8). The analytical band-limitation is indicated by the superscript 'ABL'. As depicted in Fig. 2, the resulting band-limited impulse response can be decomposed into decaying complex exponential functions and the corresponding residual. The complex exponential functions are implemented as single-pole IIR filters by using the conventional impulse invariance method [cf. (11)]. IIR filters with complex conjugate poles are typically combined (added) together and implemented as a biquad filter. The residual is modeled by an FIR filter after truncating and windowing it to a finite length L.

Note from (12) that a delay of $M \in [0, L-1]$ samples is applied to the IIR part to ensure the causality of the system. This can be implemented together with the overall delay of $\frac{r_s - R}{c}$ [cf. (9)], e.g. by replacing $z^{-(D-M)}$ with z^{-D} in Fig. 1. The noncausal part of the modal impulse response thus will not introduce additional group delay to the overall system if $M < \frac{r_s - R}{c} f_s$. For $M = 31$, $f_s = 48\,\mathrm{kHz}$ and $c = 343\,\mathrm{m/s}$, the distance from the source to the nearest point on the sphere ($r_s - R$) must be greater than $\frac{M \cdot c}{f_s} \approx 0.222\,\mathrm{m}$, which is satisfied in most configurations. Even if the source is closer than the minimum distance and the digital filter exhibits a group delay that exceeds the wave propagation delay (source to the nearest point on the sphere), the accuracy in the frequency domain will not be affected except the additional linear-phase delay.

3. NUMERICAL BAND-LIMITED IMPULSE INVARIANCE METHOD

This paper proposes a new variation of the band-limited impulse invariance method. Our objective is to find a set of FIR coefficients $d_{n,k}$ that best approximate the desired modal spectrum within the frequency range of interest ($|\omega| < \pi f_s$),

$$e^{-M T_s s} A_n(s) \overset{!}{=} z^{-M} \cdot \hat{A}_n^{(\mathrm{II})}(z) + \sum_{l=0}^{L-1} d_{n,l} z^{-l}. \qquad (13)$$

A delay of $M \cdot T_s$ seconds is applied to the continuous-time transfer function (left-hand side) for time alignment with the discrete-time system. Evaluating (13) for $s = i\omega$ and $z = e^{i\Omega} = e^{i\omega T_s}$ (corresponding to the continuous-time and discrete-time Fourier transforms) and rearranging the

terms yield

$$\sum_{l=0}^{L-1} d_{n,l}\, e^{i(M-l)\omega T_\mathrm{s}} = A_n(i\omega) - \hat{A}_n^{(\mathrm{II})}(e^{i\omega T_\mathrm{s}}). \quad (14)$$

Therefore, the FIR part should model the residual, which corresponds to the difference between the desired frequency respoinse $A_n(i\omega)$ and the frequency response of the filter designed with the impulse invariance method $\hat{A}_n^{(\mathrm{II})}(e^{i\omega T_\mathrm{s}})$ [cf. Fig. 2].

By selecting a set of control frequencies, $\omega_k = 2\pi f_k = \Omega_k T_\mathrm{s}$ for $k = 0, 1, \ldots, K-1$, (14) can be expressed in a matrix form,

$$\boldsymbol{W}\boldsymbol{d}_n = \boldsymbol{a}_n \quad (15)$$

where

$$\boldsymbol{W} = \begin{bmatrix} e^{iM\Omega_0} & e^{i(M-1)\Omega_0} & \ldots & e^{i(M-L)\Omega_0} \\ e^{iM\Omega_1} & e^{i(M-1)\Omega_1} & \ldots & e^{i(M-L)\Omega_1} \\ \vdots & \vdots & \ddots & \vdots \\ e^{iM\Omega_{K-1}} & e^{i(M-1)\Omega_{K-1}} & \ldots & e^{i(M-L)\Omega_{K-1}} \end{bmatrix}, \quad (16)$$

$$\boldsymbol{d}_n = \begin{bmatrix} d_{n,0} & d_{n,1} & \ldots & d_{n,L-1} \end{bmatrix}^\mathrm{T}, \quad (17)$$

and

$$\boldsymbol{a}_n = \begin{bmatrix} A_n(i\omega_0) - \hat{A}_n^{(\mathrm{II})}(e^{i\omega_0 T_\mathrm{s}}) \\ A_n(i\omega_1) - \hat{A}_n^{(\mathrm{II})}(e^{i\omega_1 T_\mathrm{s}}) \\ \vdots \\ A_n(i\omega_{K-1}) - \hat{A}_n^{(\mathrm{II})}(e^{i\omega_{K-1} T_\mathrm{s}}) \end{bmatrix}. \quad (18)$$

Since we are seeking for real FIR coefficients, it is sufficient to specify the desired spectrum on the positive frequency axis, i.e. $\omega_k \in [0, \pi f_\mathrm{s}]$. For $K > L$, the squared error can be minimized by the least squares solution [18, Eq. (7)],

$$\boldsymbol{d}_n^{(\mathrm{NBL})} = (\Re\{\boldsymbol{W}^\mathrm{H}\boldsymbol{W}\})^{-1}\Re\{\boldsymbol{W}^\mathrm{H}\boldsymbol{a}_n\} \quad (19)$$

where $(\cdot)^\mathrm{H}$ denotes the Hermitian transpose (conjugate transpose) of a matrix, $(\cdot)^{-1}$ the inverse of a square matrix, and $\Re\{\cdot\}$ takes the real part of the matrix entries. The number of control frequencies and their distribution are design parameters, the choice of which leads to different FIR filters. The z-transform of the resulting filter is similar to (12) but with a different FIR part,

$$\hat{A}_n^{(\mathrm{NBL})}(z) = z^{-M} \cdot \hat{A}_n^{(\mathrm{II})}(z) + \sum_{l=0}^{L-1} d_{n,l}^{(\mathrm{NBL})} z^{-l}, \quad (20)$$

where $d_{n,l}^{(\mathrm{NBL})}$ are the entries of $\boldsymbol{d}_n^{(\mathrm{NBL})}$ obtained in (19). The superscript 'NBL' indicates the numerical band limitation performed in the current approach.

4. EVALUATION

In this section, the presented approach is used for the simulation of a sound field captured on a rigid sphere with radius $R = 0.042\,\mathrm{m}$. A point source is assumed to emit a discrete-time unit impulse $\delta[n]$. The distance from the point source to the center of the sphere r_s is varied. The simulations are performed at a typical audio sampling frequency of $48\,\mathrm{kHz}$. The speed of sound is assumed to be $c = 343\,\mathrm{m/s}$.

Three different time-domain approaches are compared.

- conventional impulse invariance method which only uses IIR filters (II)
- analytical band-limited impulse invariance method, where the FIR coefficients are derived analytically (ABL)
- numerical band-limited impulse invariance method, where the FIR coefficients are obtained by least squares solution as described in Sec. 3 (NBL)

For the two band limitation approaches, the FIR length is set to $L = 15$ and the non-causal length to $M = 7$, satisfying $L = 2M + 1$. Therefore, the FIR coefficients are centered at the first sample of the IIR filter responses. For the ease of comparison, a delay of M samples is added to the conventional impulse invariance method, $z^{-M} \cdot \hat{A}_n^{(\mathrm{II})}(z)$, aligning it with the other filters in the time domain. In the analytical approach, the FIR coefficients are obtained by windowing the residual with a Kaiser-Bessel window (parameter $b = 8.6$). In the numerical approach, the control frequencies ω_k are logarithmically distributed between $2\,\mathrm{Hz}$ to $24\,\mathrm{kHz}$, which is heuristically chosen. The number of control frequencies are set to $K = 2\,L = 30$. It is assumed that the overall delay $\frac{r_\mathrm{s}-R}{c}$ is ideally simulated. We will only discuss the properties of the modal transfer functions.

The modal frequency responses are examined by evaluating the z-transforms on the unit circle $z = e^{i\omega T_\mathrm{s}}$,

$$\hat{A}_n(z)\big|_{z=e^{i\omega T_\mathrm{s}}}. \quad (21)$$

The modeling errors are defined as the deviations from the original spectrum (complex-valued in general),

$$E_n(\omega) = \hat{A}_n(e^{i\omega T_\mathrm{s}}) - e^{-i\omega M T_\mathrm{s}} \cdot A_n(i\omega), \quad (22)$$

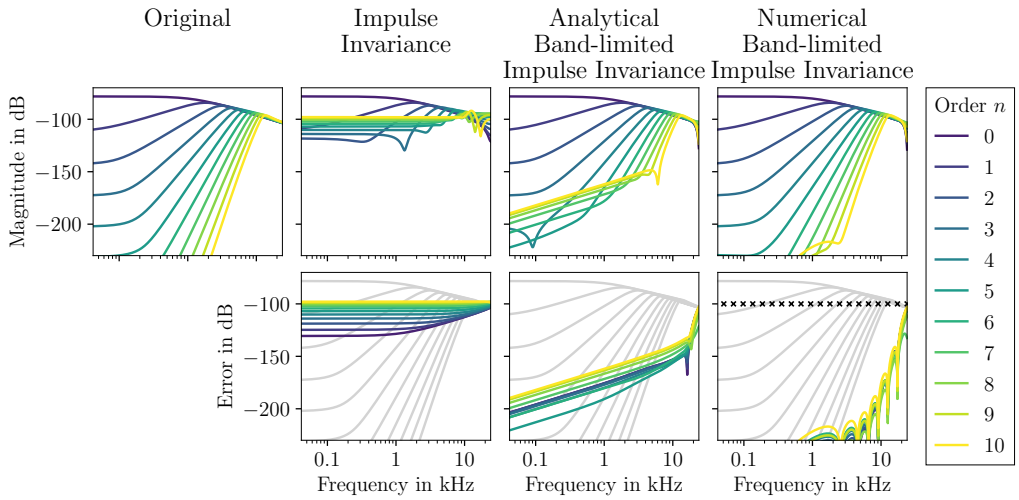

Figure 3. Frequency responses (top row) of simulated modal spectra ($R = 0.042\,\mathrm{m}$, $r_\mathrm{s} = 1\,\mathrm{m}$, $n = 0, \ldots, 10$, FIR filter length $L = 15$, non-causal part $M = 7$, $f_\mathrm{s} = 48\,\mathrm{kHz}$). The original modal spectra are shown in the top-left, and for convenience, also in the bottom row in gray. The spectral errors are shown in the bottom row. The markers $\times$ in the bottom-right plot indicate the control frequencies ω_k used in the numerical design of the FIR filters [cf. Sec. 3]. The control frequencies below the lower axis limit (42 Hz) are not shown.

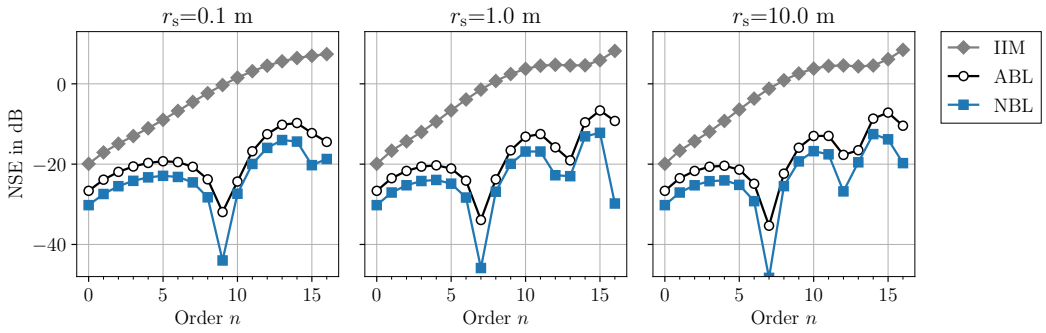

Figure 4. Normalized squared errors [cf. (23)] of the time-domain simulations ($R = 0.042\,\mathrm{m}$, $r_\mathrm{s} = 0.1\,\mathrm{m}, 1\,\mathrm{m}, 10\,\mathrm{m}$, $n = 0, \ldots, 16$, FIR filter length $L = 15$, non-causal part $M = 7$, $f_\mathrm{s} = 48\,\mathrm{kHz}$).

where the delay of M samples is accounted for. The magnitude spectra of the individual modes ($n = 0, 1, \ldots, 10$) and the corresponding spectral errors are depicted in Fig. 3. The original spectra are shown for comparison (top-left). The control frequencies are indicated by '$\times$' in the bottom-right. The limitation of the conventional impulse invariance method is apparent, where the spectral deviations increases for higher modal orders n. It can be seen that the additional FIR parts effectively reduce the errors, especially in the low frequencies. The error gradually increases as the frequency approaches the Nyquist limit $\frac{f_\mathrm{s}}{2} = 24\,\mathrm{kHz}$. The numerical approach outperforms the analytical design in a wide frequency range.

The spectral accuracy is further examined in terms of the normalized squared error (NSE)

$$\varepsilon_n = 10 \log_{10} \left[\frac{\int_{-\pi f_\mathrm{s}}^{\pi f_\mathrm{s}} |E_n(\omega)|^2 \, \mathrm{d}\omega}{\int_{-\pi f_\mathrm{s}}^{\pi f_\mathrm{s}} |A_n(i\omega)|^2 \, \mathrm{d}\omega} \right] . \qquad (23)$$

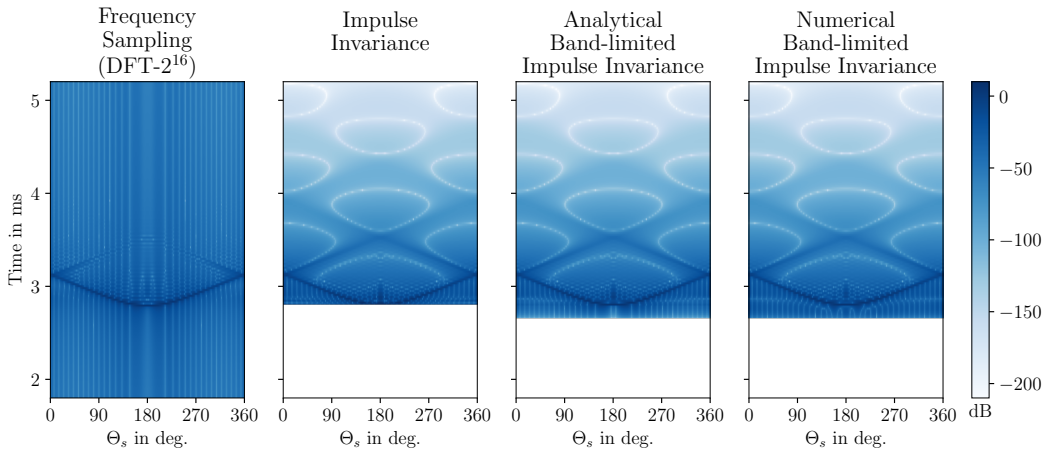

Figure 5. Directional impulse responses of a point source captured on a rigid sphere ($R = 0.042\,\mathrm{m}$, $r_\mathrm{s} = 1\,\mathrm{m}$, $\Theta_\mathrm{s} \in [0°, 360°)$, FIR filter length $L = 15$, non-causal part $M = 7$, $f_\mathrm{s} = 48\,\mathrm{kHz}$).

It represents the energy ratio between the spectral errors and the modal spectrum. The integrals in the numerator and denominator are both approximated by summing the squared magnitude spectrum at 2^{16} equally spaced frequencies (including the DC), using the discrete Fourier transform (DFT) of the coefficients. Figure 4 shows the NSE for varying source distances ($r_\mathrm{s} = 0.1, 1, 10\,\mathrm{m}$). As expected, the conventional impulse invariance method exhibits the highest errors in all cases. The improvement achieved by the band-limited impulse invariance methods in terms of NSE ranges from $6.7\,\mathrm{dB}$ to $48.8\,\mathrm{dB}$. When comparing the two band limitation approaches, the numerical method outperforms the analytical method by $3.6\,\mathrm{dB}$ on average. For these two methods, the NSE fluctuates in the same fashion depending on the modal order n and source distance r_s.

Finally, the directional impulse responses on the rigid sphere are computed by evaluating the modal expansion (9) up to the 19th order ($N = 19$). The point source is placed on the xy-plane at $r_\mathrm{s} = 1\,\mathrm{m}$ distance. The receivers are uniformly distributed on the equator, i.e. $\Theta_\mathrm{s} \in [0°, 360°)$. The impulse responses at these points represent the directional impulse responses on the entire sphere due to the axis-symmetry with respect to the direction of the point source $\boldsymbol{x}_\mathrm{s}$ [cf. (1)]. The impulse responses are depicted in Fig. 5. For comparison, the result of a frequency-domain simulation is also shown (left), where the modal spectra are uniformly sampled at 2^{16} frequencies below the Nyquist limit and transformed into the time domain by using the IDFT. The temporal smearing is apparent, which is mainly due to the hard band limitation of the modal spectrum. It is apparent that the time-domain approaches are free of such artifacts. The diffraction around the surface and the exponential decay are modeled properly, which is not the case for the frequency-domain approach. The non-causal length of the FIR filter is explicitly controlled by the design parameter M. The three time-domain methods only differ around the arrival of the first wavefront where the FIR filters are active by design (for $t \in [2.624\,\mathrm{ms}, 2.916\,\mathrm{ms}]$). It can be seen that the analytical and numerical methods lead to different temporal structure within this interval. We observed that the difference is more pronounced at high modal orders (not shown here). The distribution of the control frequency seems to influence the transients, which has to be further investigated in subsequent studies.

5. CONCLUSION

The directional impulse response on a rigid sphere is simulated with a high accuracy by using a modified version of the band-limited impulse invariance method. The analytical derivation of the FIR filter coefficients is replaced with a numerical method. For a given filter structure, the proposed method has the potential of achieving higher spectral accuracy. at the expense of increased computations only in the modeling stage. The proposed method is a suitable choice if both spectral accuracy and compact

temporal structure are of interest. It can be used in other modal signal processing applications, such as distance compensation for higher-order Ambisonics, radial filtering in spherical microphone arrays, and radiation control using compact spherical loudspeaker arrays.

The proposed numerical band-limited impulse invariance method can be extended by including frequency-dependent weights in the cost function. The spectral shape of the modeling errors can be manipulated in this way. The filter structure can be further optimized, e.g. by combining the FIR filters belonging to different modal orders into a single filter. Also, the overlap of the IIR and FIR filters in the time domain can be removed by merging the early part of the IIR into the FIR coefficients [19]. Such practical considerations are beyond the scope of this paper, and will be addressed in the future.

6. REFERENCES

[1] J. Meyer and G. Elko, "A highly scalable spherical microphone array based on an orthonormal decomposition of the soundfield," in *Proc. Int. Conf. Acoust. Speech Signal Process. (ICASSP)*.

[2] B. Rafaely, *Fundamentals of Spherical Array Processing*. Berlin, Germany: Springer, 2nd ed., 2019.

[3] F. Zotter and M. Frank, *Ambisonics*. Cham, Switzerland: Springer, 2019.

[4] B. Bernschütz, C. Pörschmann, S. Spors, and S. Weinzierl, "SOFiA sound field analysis toolbox," in *Proc. Int. Conf. Spatial Audio (ICSA)*, (Detmold, Germany), pp. 7–15, Nov. 2011.

[5] D. P. Jarrett, E. A. Habets, M. R. Thomas, and P. A. Naylor, "Rigid sphere room impulse response simulation: Algorithm and applications," *J. Acoust. Soc. Am. (JASA)*, vol. 132, pp. 1462–1472, Sept. 2012.

[6] N. Hahn, F. Schultz, and S. Spors, "Spatio-temporal properties of simulated impulse responses on a rigid sphere," in *Proc. 47th German Annu. Conf. Acoust. (DAGA)*, (Wien, Austria), pp. 836–839, Aug. 2021.

[7] H. Pomberger, "Angular and radial directivity control for spherical loudspeaker arrays," Master's thesis, University of Music and Performing Arts, Graz, Austria, 2008.

[8] F. Zotter, *Analysis and Synthesis of Sound-radiation with Spherical Arrays*. PhD thesis, University of Music and Performing Arts, Graz, Austria, 2009.

[9] S. Spors, V. Kuscher, and J. Ahrens, "Efficient realization of model-based rendering for 2.5-dimensional near-field compensated higher order Ambisonics," in *Proc. Workshop Appl. Signal Process. Audio Acoust. (WASPAA)*, (New Paltz, NY, USA), pp. 61–64, Oct. 2011.

[10] S. Lösler and F. Zotter, "Comprehensive radial filter design for practical higher-order Ambisonic recording," in *Proc. 41st German Annu. Conf. Acoust. (DAGA)*, (Nuremberg, Germany), pp. 452–455, Mar. 2015.

[11] N. Hahn, F. Schultz, and S. Spors, "Aliasing-free time-domain simulation of spherical microphone arrays," in *Proc. 49th German Annu. Conf. Acoust. (DAGA)*, (Hamburg, Germany), pp. 1620–1623, Mar. 2023.

[12] N. Hahn, F. Schultz, and S. Spors, "Band limited impulse invariance method," in *Proc. 30th Eur. Signal Process. Conf. (EUSIPCO)*, (Belgrade, Serbia), pp. 209–213, Sept. 2022.

[13] N. A. Gumerov and R. Duraiswami, *Fast Multipole Methods for the Helmholtz Equation in Three Dimensions*. Oxford, UK: Elsevier, 2005.

[14] F. W. J. Olver, D. W. Lozier, R. F. Boisvert, and C. W. Clark, *NIST Handbook of Mathematical Functions Handback*. New York, NY, USA: Cambridge University Press, 2010.

[15] T. I. Laakso, V. Välimäki, M. Karjalainen, and U. K. Laine, "Splitting the unit delay," *IEEE Signal Process. Mag.*, vol. 13, pp. 30–60, Jan. 1996.

[16] L. B. Jackson, "A correction to impulse invariance," *IEEE Signal Process. Lett.*, vol. 7, pp. 273–275, Oct. 2000.

[17] W. F. Mecklenbräuker, "Remarks on and correction to the impulse invariant method for the design of IIR digital filters," *Signal Process.*, vol. 80, pp. 1687–1690, July 2000.

[18] B. Bank, "Logarithmic frequency scale parallel filter design with complex and magnitude-only specifications," *IEEE Signal Process. Lett.*, vol. 18, pp. 138–141, Feb. 2011.

[19] B. Bank and J. O. Smith III, "A delayed parallel filter structure with an FIR part having improved numerical properties," in *Proc. of Audio Eng. Soc. (AES) Conv.*, (Berlin, Germany), Apr. 2014.